ACS APPLIED MATERIALS & INTERFACES

Self-Assembled Plasmonic Nanoparticles on Vertically Aligned Carbon Nanotube Electrodes via Thermal Evaporation

Youngmin Kim,[†,⊥] Seungjae Lee,[‡,⊥] Kyungjun Lee,[†] Sangdeok Shim,[§] Jin Young Kim,[∥]
Hyung Woo Lee,*[,∥] and Dukhyun Choi*[,†]

[†]Department of Mechanical Engineering, College of Engineering, Kyung Hee University, Yongin, 446-701, Republic of Korea
[‡]Division of Mechanical Engineering, Wonkwang University, Iksan, 570-749, Republic of Korea
[§]Department of Chemistry, Sunchon National University, 315 Maegok-dong, Sunchon 740-742, Republic of Korea
[∥]Department of Nano Fusion Technology and Department of Nanomaterials Engineering, Pusan National University, Busan, 609-735, Republic of Korea

Supporting Information

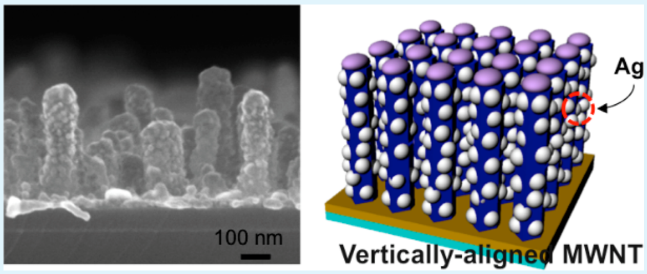

ABSTRACT: This study details the development of a large-area, three-dimensional (3D), plasmonic integrated electrode (PIE) system. Vertically aligned multiwalled carbon nanotube (VA-MWNT) electrodes are grown and populated with self-assembling silver nanoparticles via thermal evaporation. Due to the geometric and surface characteristics of VA-MWNTs, evaporated silver atoms form nanoparticles approximately 15−20 nm in diameter. The nanoparticles are well distributed on VA-MWNTs, with a 5−10 nm gap between particles. The size and gap of the self-assembled plasmonic nanoparticles is dependent upon both the length of the MWNT and the thickness of the evaporated silver. The wetting properties of water of the VA-MWNT electrodes change from hydrophilic (~70°) to hydrophobic (~120°) as a result of the evaporated silver. This effect is particularly pronounced on the VA-MWNT electrodes with a length of 1 μm, where the contact angle is altered from an initial 8° to 124°. Based on UV−visible spectroscopic analysis, plasmonic resonance of the PIE systems occurs at a wavelength of approximately 400 nm. The optical behavior was found to vary as a function of MWNT length, with the exception of MWNT with a length of 1 μm. Using our PIE systems, we were able to obtain clear surface-enhanced Raman scattering (SERS) spectra with a detection limit of ~10 nM and an enhancement factor of ~10^6. This PIE system shows promise for use as a novel electrode system in next-generation optoelectronics such as photovoltaics, light-emitting diodes, and solar water splitting.

KEYWORDS: *plasmonics, self-assembly, vertically aligned multiwalled carbon nanotube, thermal evaporation, contact angle, surface-enhanced Raman scattering*

1. INTRODUCTION

The study of plasmonics, the interaction between an electromagnetic field and free electrons, is rapidly growing due to extraordinary optical properties.[1−5] Many researchers in a variety of fields such as biology, optics, and electronics expect plasmonic-based photonic technology to provide innovative performance and progressive device efficiency.[6−10] To date, fundamental studies and various applications regarding plasmonics have been extensively studied and reported. Examples include light transfer, confinement, transmission, and scattering.[2−5] Applications in nanophotonic fields include laser beam shaping, imaging, surface-enhanced Raman scattering (SERS), solar cells, and solar water splitting.[7−10] Though the specific issues affecting plasmonic devices vary by application, the most critical consideration for all industry applications is the fabrication of large-area, cost-effective, and reproducible plasmonic systems.

There are many photoelectronic devices that consist of top/bottom electrodes with an active layer (e.g., a photoabsorption or light-emitting layer) in the middle.[11−15] A plasmonic element could be embedded either in the interface between the electrode and active layer or inside the active layer.[16−19] When plasmonic-embedded devices are fabricated, the dispersion of plasmonic nanoparticles (NPs) without agglomeration is a critical issue. Previously, our group has reported three-dimensionally (3D) distributed plasmonic NPs on zinc oxide (ZnO) nanorods through thermal deposition and a dewetting process.[20] Large-area ZnO nanorods were prepared on a gallium nitride (GaN) substrate; metal deposition and a dewetting process completed the uniformly distributed plasmonic NPs on ZnO nanorods. However, a high-temperature dewetting process over 500 °C requires thermal resistive substrates, which, in some cases, lead to deterioration of the electrical and mechanical properties of the other materials.

Received: September 3, 2014
Accepted: November 10, 2014
Published: November 10, 2014

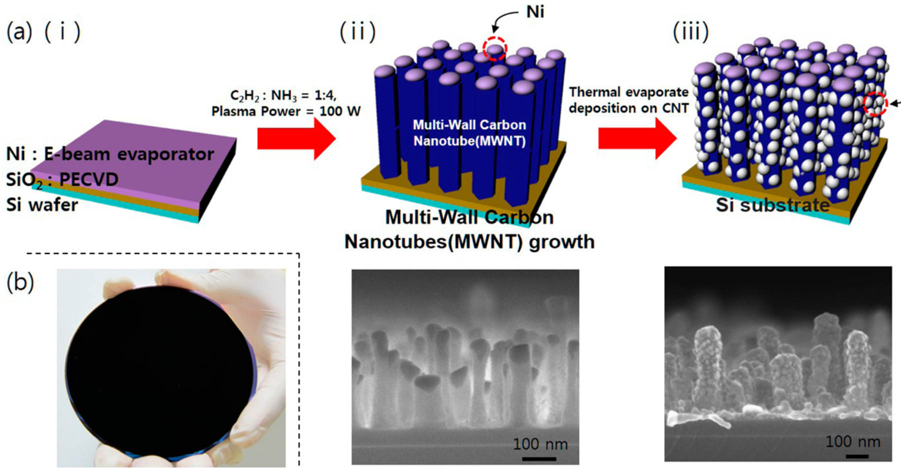

Figure 1. Fabrication process for the PIE assembly. (a) Schematic and FE-SEM images for the formation of silver NPs on VA-MWNT electrode. (b) Photograph of large-area 3D PIE on 4 in. wafer.

Therefore, the process and materials are still necessary to improve next-generation plasmonic—embedded photoelectronic devices.

Carbon nanotubes (CNTs) have attracted a great deal of attention due to their unique electrical, chemical, and mechanical properties.[21−24] CNTs have been utilized as a template material for hybridizing metal and semiconducting NPs because they have a large chemically active surface.[25−29] Metal-decorated CNT hybrid structures have been synthesized via a reduction process,[25,26] electroless deposition,[27,28] and electrodeposition[29] for various applications such as catalysts, optics, and nanobiotechnology. Depending on the application, CNTs can be aligned vertically, laterally, or randomly. Most electronic devices require laterally aligned CNTs for an electrical connection. Due to the spatial limits of nanodevices, vertically aligned CNTs (VA-CNT) are in demand for use as 3D conductive structures such as via-connectors in electronic devices. Furthermore, the growth technique of VA-CNT is critically important when using an individual carbon nanotube as an electrical connector or nanostructure in small devices. Our group has also shown the VA-CNT, developed via plasma enhanced chemical vapor deposition (PECVD), and demonstrated a CNT-tipped atomic force microscopy (AFM) probe which was fabricated via the transplanting technique.[30]

We have adopted VA-CNTs in order to improve upon our previous concept for a large-area 3D plasmonic structure,[20] as CNTs have a hydrophobic surface and the vertical geometry of VA-CNT may be effective in a 3D structure. Furthermore, CNTs can be applied in an electron transport medium for a variety of electronic devices. Herein, we introduce a large-area 3D plasmonic-integrated electrode (PIE) assembly using only the evaporation of metal on a vertically aligned multiwalled carbon nanotube (VA-MWNT) electrode. The formation of plasmonic NPs within this process does not require annealing, lending our process a critical advantage. Self-assembled plasmonic NPs on VA-MWNTs are characterized in terms of morphology, wettability, and optical properties. We examine how these characteristics depend on the length of the MWNT and the thickness of silver. The plasmonic performance of our PIE assembly is measured through SERS signals. We believe that our PIE assembly is a promising building block for next-generation optoelectronic nanodevices.

2. EXPERIMENTAL SECTION

2.1. VA-MWNT Growth. In general, CNTs are synthesized in three steps: the decomposition of hydrocarbon gas (in this study, acetylene (C_2H_2) was used) via high temperature and plasma, the diffusion of carbon atoms along the surface and through the bulk of a catalytic island (in this study, nickel (Ni)), and the precipitation of carbon atoms between a catalytic island and a diffusion barrier.[31] Here, VA-MWNTs were synthesized via direct current plasma-enhanced chemical vapor deposition (DC-PECVD). Ni was used to form a catalytic metal layer 7 nm in thickness deposited on the SiO_2/Si substrate via e-beam evaporator. The catalytic-layer-deposited substrate was loaded onto the heater in a vacuum chamber, and the temperature was gradually increased to 650 °C. At 650 °C, ammonia, as an etching gas, was flushed into the chamber, and a 60 W plasma was generated for 5 min. The temperature of the heater was then increased to 750 °C and the active gas with a NH_3/C_2H_2 ratio of 4:1 was injected into the chamber. The power of the plasma was then increased to 100 W, and the time that the 100 W plasma was applied is referred to as the MWNT growth time. MWNTs with lengths of 150, 250, 500, and 1000 nm were synthesized under various MWNT growth times. Following the MWNT growth, the plasma was turned off and the heater was slowly cooled to prevent damage to the MWNTs.

2.2. 3D FDTD Simulation. We calculated the electric field distributions on VA-MWNTs both with and without silver NPs using the finite-difference time-domain (FDTD) simulation (Lumerical FDTD Solutions). The optical information on MWNTs followed a previous literature.[32] The unit cell consists of one VA-MWNT on SiO_2 and silver NPs (Supporting Information, Figure S1). In detail, a VA-MWNT with 250 nm in length and 100 nm in diameter was modeled on a SiO_2 substrate. The diameter of the silver NPs was approximately 15 nm, and they were positioned with a gap of approximately 8 nm. The unit cell was embedded in air with periodic boundary conditions at the sidewalls. In this simulation, the incident light was directed normal to the sample surface and was polarized perpendicularly to the propagation direction.

2.3. Microscopic and Optical Observation. The surface morphologies were characterized using field emission scanning electron microscopy (FE-SEM; Carl Zeiss, LEO SUPRA 55) and transmission electron microscopy (TEM; JEOL, JEM-ARM200F). A UV−visible photospectrometer (JASCO) was used to measure the reflectance of the samples. SERS spectra were measured via the Raman system (JASCO, NRS-2100) with an excitation wavelength of 532 nm, where the integration time was 4 s, 10 times. The chemical target was rhodamine 6G (R6G).

3. RESULTS AND DISCUSSION

3.1. Plasmonic-Integrated Electrode (PIE) Assembly. Figure 1 shows the fabrication process for the PIE assembly. First, we grew VA-MWNTs on a SiO_2/Si wafer via DC-PECVD (see the Experimental Section). After preparing the VA-MWNT electrode, we deposited silver using a thermal evaporator. Interestingly, the evaporated silver atoms self-assembled NPs on the VA-MWNTs (see the schematic and FE-SEM images in Figure 1a,iii). We attributed this self-assembly of silver NPs on the VA-MWNTs to the surface and geometrical characteristics of MWNTs. Because the VA-MWNT electrode can be fabricated at the wafer scale, such as the 4 in. wafer used here and depicted in Figure 1b, we could create a large-area 3D PIE assembly. Our PIE assembly fabrication process is simple, cost-effective, and high-throughput, resulting in a PIE platform that is a promising building block for next-generation nanophotonic devices.

As mentioned above, we found that silver atoms exposed to thermal evaporation do not form a film but self-assembled NPs on VA-MWNTs (see the FE-SEM and TEM images in Figure 2a,b). The spacing between adjacent lattice planes in the self-assembled silver NP was 0.234 nm, indicating the preferential growth of the silver NPs along the (111) orientation (see the high-resolution TEM image inset in Figure 2b). We attribute such a self-assembly of silver atoms to the surface characteristics and vertically aligned geometry of MWNTs. Generally, the surface of a MWNT is hydrophobic due to the low surface energy, which results in poor coverage by other materials. Thus, metal islands are easily created on the MWNT surface. Furthermore, when the MWNTs are vertically aligned, additional evaporated atoms continue to form NPs on the VA-MWNTs. We compared the morphology of evaporated silver with a thickness of 30 nm on laterally organized MWNTs (LO-MWNTs) and VA-MWNTs, as shown in Figure S2 (Supporting Information). The formation of silver NPs on VA-MWNTs is clearly visible. On the other hand, silver atoms on LO-MWNTs formed disconnected films. This formation stems from the hydrophobic characteristic of the MWNTs, as well as the agglomerating property of silver atoms.[33,34] As a result, we conclude that the geometry and material characteristics of MWNTs and silver lead to the formation of self-assembled plasmonic NPs on a VA-MWNT electrode.

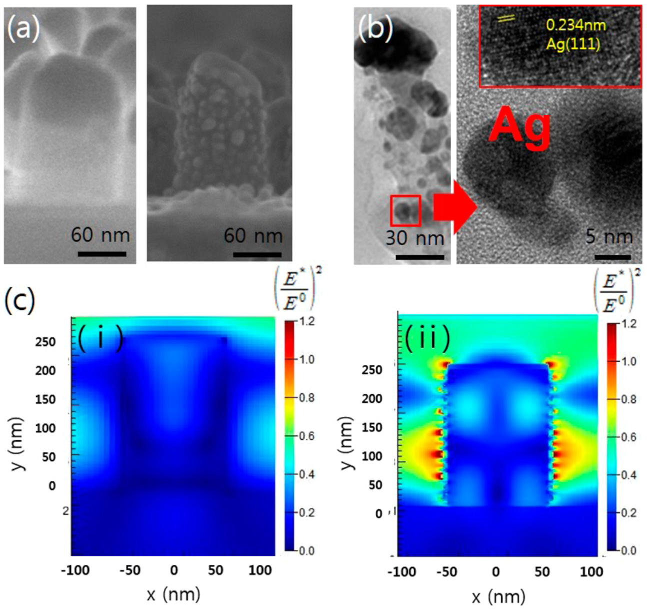

Figure 2. Morphological and electric field characterization for VA-MWNT with and without silver NPs. (a) FE-SEM and (b) TEM images for self-assembled silver NPs on VA-MWNT. (c) Electric field distribution on VA-MWNT (i) with and (ii) without silver NPs.

We have found that silver NPs on VA-MWNTs play a critical role in electric field enhancement via localized surface plasmons. Figure 2c shows the electrical field distributions on VA-MWNTs both with and without silver NPs using 3D computational electrodynamic calculations based on the FDTD method. The simulation details were provided in the Experimental Section. As shown in Figure 2c,i, a VA-MWNT without silver NPs does not provide any enhanced electrical fields, while the VA-MWNT with silver NPs (referred to as a PIE in this study) shows clearly enhanced electric fields around the silver NPs interfacing with VA-MWNTs due to the localized surface plasmons on the silver NPs. Such an enhanced electric field improves the light absorption and carrier transport at the interface, making the PIE platform a great building block for photonic devices such as solar cells, LEDs, and solar water splitters.

Figure 3 shows the FE-SEM images of VA-MWNT electrodes with average lengths (L_{MWNT}) of 150, 250, 500, and 1000 nm, both before and after the evaporation of silver with a thickness of 30 nm. We deposited silver on VA-MWNT electrodes with thicknesses (t_{Ag}) of 20, 30, and 50 nm, as shown in Figure S3 (Supporting Information). The FE-SEM images clearly show an even distribution of silver NPs on the VA-MWNTs. According to the length of the MWNTs, except the length of 1000 nm, the diameter (D_{Ag}) of the silver NPs is approximately 15−20 nm, and the gap (G_{Ag}) between the NPs is less than 10 nm (Figure 4a). The error bar is the standard deviation of each value. The size of silver NPs on the MWNTs with the length of 1000 nm was various up to ∼100 nm (Figure S4, Supporting Information). This size and gap of silver NPs could be effective for plasmonic local field enhancement and plasmonic resonance based on position. By increasing the thickness of evaporated silver from 20 to 50 nm, the size of the silver NPs was slightly increased (approximately 15 nm), and the gap between NPs slightly decreased (Figure 4b).

3.2. Wettability of the PIE Assembly. We examined the wettability of the PIE assembly as a function of the thickness of the evaporated silver and length of the MWNTs, as shown in Figure 5. Because MWNTs are essentially hydrophobic, they typically show a contact angle (CA) greater than 90°.[35,36] However, the VA-MWNTs exhibit a CA of less than 90° prior to silver evaporation due to the vertically aligned geometry of the MWNTs. The CA of VA-MWNTs with a length of 1000 nm is approximately 8°, which is a superhydrophilic characteristic. It can thus be easily understood that surface geometry is a critical factor for the determination of CA. Interestingly, silver evaporation increased all of the CAs to over 90°, some reaching approximately 120°, though silver also has a hydrophilic character, with an average CA of 70−80°.[37,38] We attribute the change in CA to interfacial effects such as pinning, though this aspect remains an area for further study.

3.3. Optical Characterizations. Figure 6 shows the absorption behaviors of PIE assemblies. The absorption spectra differ according to the length of the MWNTs without silver NPs due to the scattering and interference effects (Figure 6a). After silver evaporation, the absorption spectra were found to

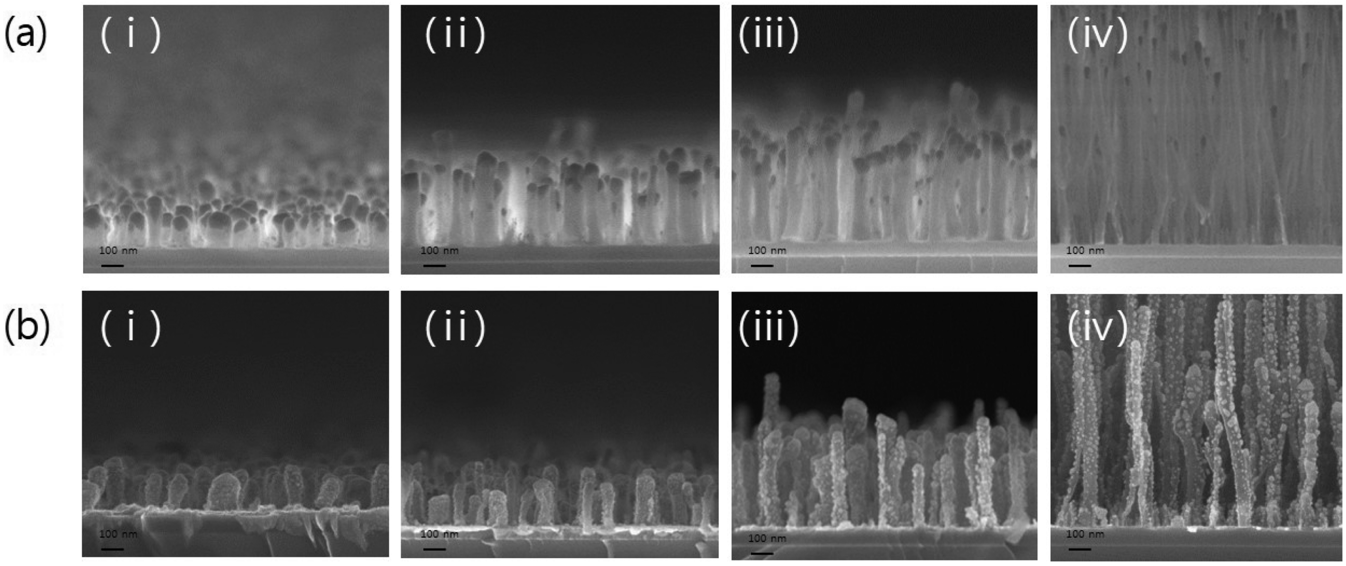

Figure 3. FE-SEM images of VA-MWNTs with average lengths of (i) 150, (ii) 250, (iii) 500, and (iv) 1000 nm (a) before and (b) after the evaporation of silver with a thickness of 30 nm. Different length of MWNTs and self-assembled silver NPs can be clearly seen.

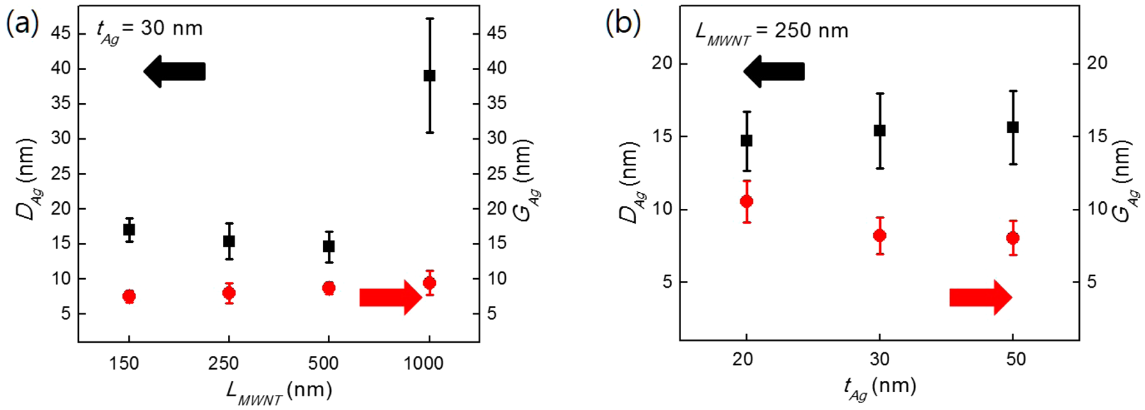

Figure 4. The diameter (D_{Ag}) of self-assembled silver NPs and the gap (G_{Ag}) between the NPs according to (a) the length of the MWNTs (L_{MWNT}) and (b) silver thickness (t_{Ag}). The values are average and the error bars are standard deviation for each value.

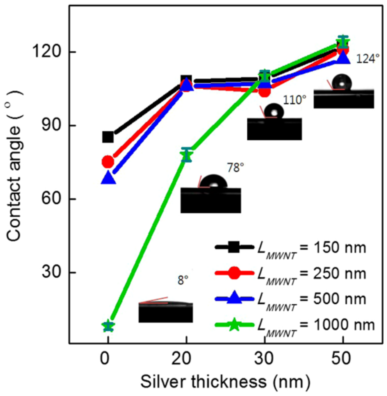

Figure 5. Wettability of the PIE assembly. The graph shows the behaviors of contact angle of the PIE assembly as a function of the thickness of the evaporated silver and length (L_{MWNT}) of the MWNTs.

be similar for different silver thicknesses, and the maximum absorption positions were found around 400 nm (Figure 6b). We attribute the similar absorption positions to the localized surface plasmon resonance (LSPR) of silver NPs with a diameter of ~15 nm.[39−41] The maximum absorption of around 400 nm could be found for short MWNTs where L_{MWNT} = 150, 250, and 500 nm. The maximum absorption of L_{MWNT} = 1000 nm was observed suddenly around 550 nm, indicating larger silver NPs on VA-MWNT. Large, aggregated silver NPs (50–100 nm) can be observed in the FE-SEM image of Figure S4 (Supporting Information).

3.4. SERS Performance. We investigated the plasmonic enhancement of our PIE assemblies through the SERS performance. First, the dependency of SERS intensities on the thickness of the silver layer (t_{Ag}) was examined on the VA-MWNTs with L_{MWNT} = 250 nm, and the maximum SERS signal was obtained at t_{Ag} = 30 nm (Figure 7a). The SERS intensities were then measured according to the length of MWNT (L_{MWNT}) at t_{Ag} = 30 nm. As shown in Figure 7b, the maximum SERS signal was obtained at L_{MWNT} = 250 nm. Finally, we investigated the detection limit and SERS enhancement factor (EF) for the PIE assembly with t_{Ag} = 30 nm and L_{MWNT} = 250 nm. We were able to measure the SERS spectra of R6G at low concentrations up to 10 nM (Figure 7c and Figure S5, Supporting Information). Analytical EF was calculated via the equation EF = $(I_{SERS}/I_{Raman}) \times (C_{Raman}/C_{SERS})$, where I and C denote intensity and concentration, respectively.[42] Based on the measured results and reference data (Figure S5, Supporting

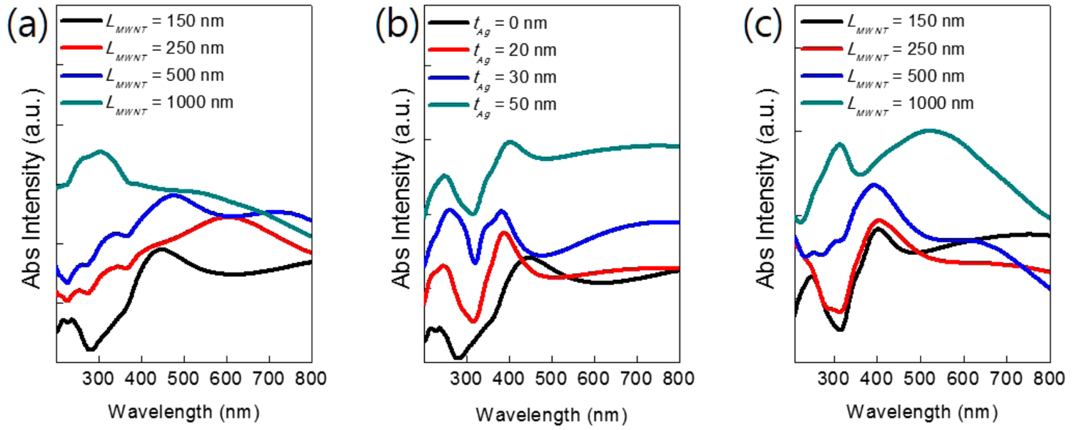

Figure 6. Absorption behaviors of PIE assemblies. (a) VA-MWNTs for different lengths (L_{MWNT}) without silver NPs. (b) Different silver thicknesses (t_{Ag}) on VA-MWNT with the length of 150 nm. (c) Different lengths of VA-MWNTs with a silver thickness of 50 nm.

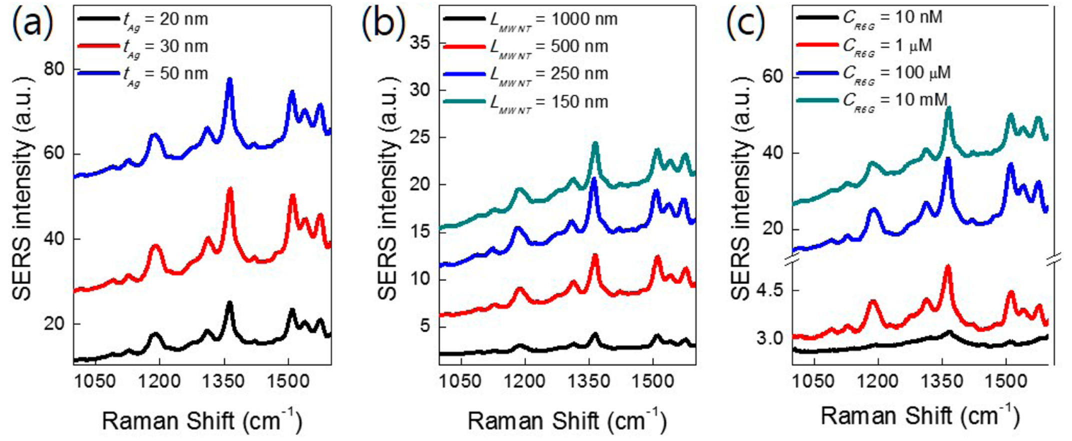

Figure 7. SERS analysis for self-assembled silver NPs on VA-MWNTs. (a) Different silver thicknesses (t_{Ag}) on the VA-MWNTs with a length (L_{MWNT}) of 250 nm. (b) Length variations (L_{MWNT} = 150, 250, 500, and 1000 nm) of VA-MWNTs with t_{Ag} = 30 nm. (c) Detection limit of SERS signals on PIE assembly with t_{Ag} = 30 nm and L_{MWNT} = 250 nm.

Information), the analytical EF was determined to reach approximately 10^6. SERS signals were measured from the minimum three different samples, over two different positions on one sample, and more than 10 times at each position. As shown in Figure S6 (Supporting Information), the SERS signals from our samples were quite uniform. Based on the SERS performance, our PIE assembly shows potential for application in next-generation photonic nanodevices for enhancing device efficiency.

4. CONCLUSIONS

We have successfully demonstrated a large-area 3D PIE assembly based on a VA-MWNT electrode and the thermal evaporation of silver. Our data clearly demonstrate that the silver atoms directly created silver NPs on the VA-MWNTs as a result of surface characteristics and the geometry of the MWNTs, as well as the agglomerating properties of the silver atoms. The silver NPs on the VA-MWNTs measured approximately 15−20 nm in diameter (up to 100 nm for L_{MWNT} = 1000 nm) with a gap of less than 10 nm, which is an effective geometry for plasmonic field enhancement. The wetting property of VA-MWNTs was changed from hydrophilic to hydrophobic (∼120°) via the evaporating silver. Based on UV−visible spectroscopic analysis, the plasmonic absorption of our PIE assemblies was found at a wavelength of approximately 400 nm. The PIE assembly shows similar optical behaviors that varied as a function of the length of the MWNT, with the exception of L_{MWNT} = 1000 nm. We provided the summarized table (Table S1, Supporting Information) of our results according to the experimental parameters in the Supporting Information. Finally, we were able to obtain clear SERS spectra from our PIE systems where the detection limit and EF were 10 nM and $\sim 10^6$, respectively. We expect that our PIE platform will be a novel building block for an advanced electrode in future optoelectronic nanodevices.

■ ASSOCIATED CONTENT

Ⓢ Supporting Information

Simulation details; FE-SEM images of LO-MWNT and VA-MWNT; size distribution of the self-assembled NP; SERS data for detection limit, reference, and uniformity; and summarized table. This material is available free of charge via the Internet at http://pubs.acs.org.

■ AUTHOR INFORMATION

Corresponding Authors

*Phone: +82-31-201-3320. E-mail: dchoi@khu.ac.kr
*Phone: +82-51-510-3160. E-mail: LHW2010@pusan.ac.kr

Author Contributions

$^{\perp}$These authors contributed equally.

Notes

The authors declare no competing financial interest.

■ ACKNOWLEDGMENTS

This work was financially supported by Wonkwang University in 2014.

■ REFERENCES

(1) Krenn, J. R.; Weeber, J. C.; Dereux, A.; Bourillot, E.; Goudonnet, J. P.; Schider, B.; Leitner, A.; Aussenegg, F. R.; Girard, C. Direct Observation of Localized Surface Plasmon Coupling. *Phys. Rev. B: Condens. Matter Mater. Phys.* **1999**, *60*, 5029−5033.

(2) Ditlbacher, H.; Krenn, J. R.; Schider, G.; Leitner, A.; Aussenegg, F. R. Two-Dimensional Optics with Surface Plasmon Polaritons. *Appl. Phys. Lett.* **2002**, *81*, 1762−1764.

(3) Kelly, K. L.; Coronado, E.; Zhao, L. L.; Schatz, G. C. The Optical Properties of Metal Nanoparticles: The Influence of Size, Shape, and Dielectric Environment. *J. Phys. Chem. B* **2003**, *107*, 668−677.

(4) Barnes, W. L.; Dereux, A.; Ebbesen, T. W. Surface Plasmon Subwavelength Optics. *Nature* **2003**, *424*, 824−830.

(5) Marzan, L. M. Tailoring Surface Plasmons through the Morphology and Assembly of Metal Nanoparticles. *Langmuir* **2006**, *22*, 32−41.

(6) Lakowicz, J. R. Plasmonics in Biology and Plasmon-Controlled Fluorescence. *Plasmonics* **2006**, *1*, 5−33.

(7) Sharma, M.; Pudasaini, P. R.; Ruiz, F.; Elam, D.; Ayon, A. A. Ultrathin, Flexible Organic−Inorganic Hybrid Solar Cells Based on Silicon Nanowires and PEDOT:PSS. *ACS Appl. Mater. Interfaces* **2014**, *6*, 4356−4363.

(8) Akimov, Y. A.; Koh, W. S. Resonant and Nonresonant Plasmonic Nanoparticle Enhancement for Thin-Film Silicon Solar Cells. *Nanotechnology* **2010**, *21*, 235201(1)−235201(6).

(9) Lee, J.; Mubeen, S.; Ji, X.; Stucky, G. D.; Moskovits, M. Plasmonic Photoanodes for Solar Water Splitting with Visible Light. *Nano Lett.* **2012**, *12*, 5014−5019.

(10) Choi, D. H.; Shin, C. K.; Yoon, D. S.; Chung, D. S.; Jin, Y. W.; Lee, L. P. Plasmonic Optical Interference. *Nano Lett.* **2014**, *14*, 3374−3381.

(11) Ferry, V. E.; Sweatlock, L. A.; Pacifici, D.; Atwater, H. A. Plasmonic Nanostructure Design for Efficient Light Coupling into Solar Cells. *Nano Lett.* **2008**, *8*, 4391−4397.

(12) Wu, X.; Liu, L.; Choy, W. C. H.; Yu, T.; Cai, P.; Gu, Y.; Xie, Z.; Zhang, Y.; Du, L.; Mo, Y.; Xu, S.; Ma, Y. Substantial Performance Improvement in Inverted Polymer Light-Emitting Diodes via Surface Plasmon Resonance Induced Electrode Quenching Control. *ACS Appl. Mater. Interfaces* **2014**, *6*, 11001−11006.

(13) Wang, W. C.; Lin, C. W.; Chen, H. J.; Chang, C. W.; Huang, J. J.; Yang, M. J.; Tjahjono, B.; Huang, J. J.; Hsu, W. C.; Chen, M. J. Surface Passivation of Efficient Nanotextured Black Silicon Solar Cells Using Thermal Atomic Layer Deposition. *ACS Appl. Mater. Interfaces* **2013**, *5*, 9752−9759.

(14) Atwater, H. A.; Polman, A. Plasmonics for Improved Photovoltaic Devices. *Nat. Mater.* **2010**, *9*, 205−213.

(15) Morfa, A. J.; Rowlen, K. L. Plasmon-Enhanced Solar Energy Conversion in Organic Bulk Heterojunction Photovoltaics. *Appl. Phys. Lett.* **2008**, *92*, 013504(1)−013504(3).

(16) Zhaoab, Y.; Burda, C. Development of Plasmonic Semiconductor Nanomaterials with Copper Chalcogenides for a Future with Sustainable Energy Materials. *Energy Environ. Sci.* **2012**, *5*, 5564−5576.

(17) Gangishetty, M. K.; Lee, K. E.; Scott, R. W. J.; Kelly, T. L. Plasmonic Enhancement of Dye Sensitized Solar Cells in the Red-to-near-Infrared Region using Triangular Core−Shell Ag@SiO$_2$ Nanoparticles. *ACS Appl. Mater. Interfaces* **2013**, *5*, 11044−11051.

(18) Kulkarni, A. P.; Noone, K. M.; Munechika, K.; Guyer, S. R.; Ginger, D. S. Plasmon-Enhanced Charge Carrier Generation in Organic Photovoltaic Films Using Silver Nanoprisms. *Nano Lett.* **2010**, *10*, 1501−1505.

(19) Ferry, V. E.; Verschuuren, M. A.; Li, H. B. T.; Verhagen, E.; Walters, R. J.; Schropp, R. E. I.; Atwater, H. A.; Polman, A. Light Trapping in Ultrathin Plasmonic Solar Cells. *Opt. Express* **2010**, *18*, A237−A245.

(20) Yoo, J. H.; Kim, J. H.; Lee, K. J.; Lee, S. M.; Kim, S. H.; Park, H. K.; Kim, S. W.; Bae, J. H.; Park, J. J.; Choi, D. H. Dewetted Gold Nanoparticles on ZnO Nanorods for Three-Dimensionally Distributed Plasmonic Hot Spots. *Scr. Mater.* **2013**, *69*, 654−657.

(21) Jonsson, L. M.; Axelsson, S.; Nord, T.; Viefers, S.; Kinaret, J. M. High-Frequency Properties of a CNT-based Nanorelay. *Nanotechnology* **2004**, *15*, 1497−1502.

(22) Li, J.; Ma, P. C.; Chow, W. S.; To, C. K.; Tang, B. Z.; Kim, J. K. Correlations between Percolation Threshold, Dispersion State, and Aspect Ratio of Carbon Nanotubes. *Adv. Funct. Mater.* **2007**, *17*, 3207−3215.

(23) Garibaldi, S.; Brunelli, C.; Bavastrello, V.; Ghigliotti, G.; Nicolini, C. Carbon Nanotube Biocompatibility with Cardiac Muscle Cells. *Nanotechnology* **2006**, *17*, 391−397.

(24) Yu, M. F.; Dyer, M. J.; Skidmore, G. D.; Rohrs, H. W.; Lu, X. K.; Ausman, K. D.; Ehr, J. R. V.; Ruoff, R. S. Three-Dimensional Manipulation of Carbon Nanotubes under a Scanning Electron Microscope. *Nanotechnology* **1999**, *10*, 244−252.

(25) Ang, L. M.; Hor, T. S. A.; Xu, G. Q.; Tung, C. H.; Zhao, S.; Wang, J. L. S. Electroless Plating of Metals onto Carbon Nanotubes Activated by a Single-Step Activation Method. *Chem. Mater.* **1999**, *11*, 2115−2118.

(26) Kim, H. S.; Lee, H.; Han, K. S.; Kim, J. H.; Song, M. S.; Park, M. S.; Lee, J. Y.; Kang, J. K. Hydrogen Storage in Ni Nanoparticle-Dispersed Multiwalled Carbon Nanotubes. *J. Phys. Chem. B* **2005**, *109*, 8983−8986.

(27) Qu, L.; Dai, L. Substrate-Enhanced Electroless Deposition of Metal Nanoparticles on Carbon Nanotubes. *J. Am. Chem. Soc.* **2005**, *127*, 10806−10807.

(28) Quinn, B. M.; Dekker, C.; Lemay, S. G. Electrodeposition of Noble Metal Nanoparticles on Carbon Nanotubes. *J. Am. Chem. Soc.* **2005**, *127*, 6146−6147.

(29) Day, T. M.; Unwin, P. R.; Wilson, N. R.; Macpherson, J. V. Electrochemical Templating of Metal Nanoparticles and Nanowires on Single-Walled Carbon Nanotube Networks. *J. Am. Chem. Soc.* **2005**, *127*, 10639−10647.

(30) Kim, S. H.; Lee, H. W.; Kim, S. G. Transplanting Assembly of Carbon Nanotube-Tipped Atomic Force Microscope Probes. *Appl. Phys. Lett.* **2009**, *94*, 193102(1)−193102(3).

(31) Teo, K. B. K.; Lee, S. B.; Chhowalla, M.; Semet, V.; Binh, V. T.; Groening, O.; Castignolles, M.; Loiseau, A.; Pirio, G.; Legagneux, P.; Pribat, D.; Hasko, D. G.; Ahmed, H.; Amaratunga, G. A. J.; Milne, W. I. Plasma Enhanced Chemical Vapour Deposition Carbon Nanotubes/Nanofibres—How Uniform do They Grow? *Nanotechnology* **2003**, *14*, 204−211.

(32) Hecht, D. S.; Thomas, D.; Hu, L.; Ladous, C.; Lam, T.; Park, Y. B.; Irvin, G.; Drzaic, P. Carbon-Nanotube Film on Plastic as Transparent Electrode for Resistive Touch Screens. *J. Soc. Inf. Disp.* **2009**, *17*, 941−946.

(33) Sharma, S. K.; Spitz, J. Hillock Formation, Hole Growth, and Agglomeration in Thin Silver Films. *Thin Solid Films* **1980**, *65*, 339−350.

(34) Sharma, S. K.; Spitz, J. Hillock Growth and Agglomeration in Thin Silver Films. *Thin Solid Films* **1979**, *61*, L13−L15.

(35) Lobo, A. O.; Ramos, S. C.; Antunes, E. F.; Marciano, F. R.; Airoldi, V. J.; Corat, E. J. Fast Functionalization of Vertically Aligned Multiwalled Carbon Nanotubes Using Oxygen Plasma. *Mater. Lett.* **2012**, *70*, 89−93.

(36) Liu, H.; Zhaia, J.; Jiang, L. Wetting and Anti-Wetting on Aligned Carbon Nanotube Films. *Soft Matter* **2006**, *2*, 811−821.

(37) Gadre, K. S.; Alford, T. L. Contact Angle Measurements for Adhesion Energy Evaluation of Silver and Copper Films on Parylene-*n* and SiO$_2$ Substrates. *J. Appl. Phys.* **2003**, *93*, 919−923.

(38) Laibinis, P. E.; Whitesides, G. M. ω-Terminated Alkanethiolate Monolayers on Surfaces of Copper, Silver, and Gold Have Similar Wettabilities. *J. Am. Chem. Soc.* **1992**, *114*, 1990−1995.

(39) Awazu, K.; Fujimaki, M.; Rockstuhl, C.; Tominaga, J.; Murakami, H.; Ohki, Y.; Yoshida, N.; Watanabe, T. A Plasmonic Photocatalyst Consisting of Silver Nanoparticles Embedded in Titanium Dioxide. *J. Am. Chem. Soc.* **2008**, *130*, 1676−1680.

(40) Vodnik, V. V.; Bo; ani; Du; an, K.; Bibi; Nata; aponji; V, Z.; Nedeljkovi; M, J. Optical Properties of Shaped Silver Nanoparticles. *J. Nanosci. Nanotechnol.* **2008**, *8*, 3511−3515.

(41) Sharma, M.; Pudasaini, P. R.; Ruiz-Zepeda, F.; Elam, D.; Ayon, A. A. Ultrathin, Flexible Organic−Inorganic Hybrid Solar Cells Based on Silicon Nanowires and PEDOT:PSS. *ACS Appl. Mater. Interfaces* **2014**, *6*, 4356−4363.

(42) Choi, D.; Choi, Y.; Hong, S.; Kang, T.; Lee, L. P. Self−Organized Hexagonal−Nanopore SERS Array. *Small* **2010**, *6*, 1741−1744.